RSC Advances

PAPER

View Article Online
View Journal | View Issue

Cite this: *RSC Adv.*, 2019, **9**, 17891

One-step electrodeposition of cerium-doped nickel hydroxide nanosheets for effective oxygen generation†

Gang Fang,[a] Jinhua Cai,[b] Zhipeng Huang *[c] and Chi Zhang [c]

Received 10th April 2019
Accepted 29th May 2019

DOI: 10.1039/c9ra02682g

rsc.li/rsc-advances

Efficient electrocatalysts catalyzing oxygen evolution reaction (OER) in alkaline media is highly desirable for large-scale hydrogen production from water splitting. Here we report the direct electrodeposition of cerium-doped nickel hydroxide nanosheets on carbon fiber paper and its prominent performance in catalyzing the OER. The composite generates a current density of 100 mA cm^{-2} at an overpotential of 320 mV, rivaling the performance of most reported OER catalysts and commercially available RuO_2. X-ray photoelectron spectroscopy analysis shows strong electronic interaction between $Ni(OH)_2$ and CeO_2, making a great contribution to the OER enhancement.

Introduction

The fast-growing world population results in a significant increase in energy consumption. Due to the limited resource of fossil energy, the development of new technologies to provide clean, affordable, and renewable energy is urgently required.[1,2] In the current hydrocarbon economic transformation, hydrogen is being actively promoted as a future energy carrier.[3] In particular, electrochemical water splitting is being regarded as a green and sustainable route to convert water into hydrogen.[3–5] However, because of the oxidative half-reaction, the oxygen evolution reaction (OER), is a 4-electron process that forms only one oxygen molecule, the kinetics of the OER is sluggish, and the OER has always been thought as the rate-limiting step in water splitting.[6–9] Therefore, there is a need to develop an effective OER electrocatalyst, which possesses lower overpotential, faster catalytic kinetics, and therefore improves the energy conversion efficiency.[10,11] Among many reported OER catalysts, RuO_2 and IrO_2 are the most active OER electrocatalysts, however, their scarcity and high cost greatly limit their large-scale applications.[12,13] Substantial advances have been made in exploiting nonprecious oxygen-evolving catalysts, among which some transition metal hydr(oxy)oxides/oxides show superior intrinsic activity.[14–19]

In general, doping catalysts with foreign elements can effectively modify electronic structure and reliably introduce defects to facilitate the adsorption and conversion of active intermediates with a lower energy barrier for OER.[20] Transition metals, especially 3d transition metals such as Fe, Mn, Cr, and Co are widely used as dopants to regulate the chemical state of electrocatalysts.[21–26] Recently, several groups reported the improvement of the performance of catalysts in hydrogen and oxygen generation by doping cerium into the host catalyst or constructing a heterogeneous structure between CeO_2 and the active catalysts.[27–34] For instance, CeO_2-cluster-doped NiO shows better performance in the OER than CeO_2 cluster surface-loaded NiO, due to promoted oxygen storage capacity and modified electronic structure of the active sites.[35] The promotion of FeOOH catalysts for OER by the integration of CeO_2 has been demonstrated due to the larger oxygen storage capacity of CeO_2 and electron interaction between CeO_2 and electrocatalysts.[30] Another work has been represented by depositing a protective thin CeO_2 layer on $NiFeO_x$ to improve stability by preventing ion leaching.[36] We have also demonstrated that the introduction of Ce induced the amorphourization of CoO_x and brought new oxygen defects.[37] Although various approaches have been developed to introduce cerium into host catalysts, a convenient method for the one-step synthesis of metal hydr(oxy)oxides/oxides catalysts remains definitely unexploited.

In this study, we reported a convenient fabrication of OER electrocatalyst by one-step electrodeposition of cerium doped nickel hydroxide nanosheets (NSs) on carbon fiber paper (CFP) and its effective catalytic activity in the OER. The electrodeposited freestanding electrode possesses advantageous active site utilization and simple fabrication over conventional powder electrocatalysts, which is physically

[a]School of Chemistry and Chemical Engineering, Jiangsu University, Zhenjiang, 212013, P. R. China

[b]College of Chemistry & Chemical Engineering, Jinggangshan University, Jian, Jiangxi Province 343009, P. R. China

[c]School of Chemical Science and Engineering, Tongji University, Shanghai, 200092, P. R. China. E-mail: zphuang@tongji.edu.cn

† Electronic supplementary information (ESI) available. See DOI: 10.1039/c9ra02682g

mixed with polymeric binder and conducting agent to make a slurry for coating on current collector.[38] The optimization of the molar ratio of Ni to Ce in the deposition solution revealed that a 30 : 1 Ni : Ce solution generated a film with the best performance. With the introduction of Ce, the optimized $Ni(OH)_2 \cdot 0.75H_2O$–CeO_2 NSs showed an tremendous increase in OER performance with the lowest overpotential of 320 mV at 100 mA cm^{-2} and Tafel slope of 126 mV dec^{-1} in alkaline electrolyte, as compared with that of $Ni(OH)_2 \cdot 0.75H_2O$ NSs(η_{100} = 460 mV, Tafel slope = 185 mV dec^{-1}) deposited by the same method. Meanwhile, the $Ni(OH)_2 \cdot 0.75H_2O$–CeO_2 NS showed prominent stability at a high reaction rate for a long time and the faradaic efficiency of 92% during water oxidation. These results not only present a new 3d transition metal hydroxide doped with cerium as an effective OER catalysts, but also introduce a facile method for one step electrodeposition synthesis of electrocatalysts loaded onto conductive support.

Experimental

Reagents

Nickel nitrate hexahydrate ($Ni(NO_3)_2 \cdot 6H_2O$, AR), cerium nitrate hexahydrate ($Ce(NO_3)_3 \cdot 6H_2O$, REO), acetone (CH_3COCH_3, AR), and ethanol (C_2H_5OH, AR) were purchased from Tansoole Co., Ltd. CFP was commercially available from Hesen Co., Ltd. All chemicals were used as received without further purification.

Synthesis

Prior to synthesis, a few pieces of CFP (1 cm × 2 cm) were washed ultrasonically with acetone, ethanol, and deionized water every 10 minutes in sequence. $Ni(OH)_2 \cdot 0.75H_2O$–CeO_2 NSs were directly electrodeposited on the CFP in a three-electrode cell, using the CFP as the working electrode, Pt as the counter electrode, and Hg/Hg_2Cl_2 as the reference electrode. The electrolyte solutions with different atomic ratio of Ni to Ce were prepared by mixing 10 mmol $Ni(NO_3)_2 \cdot 6H_2O$ with different amounts of $Ce(NO_3)_3 \cdot 6H_2O$ (*i.e.*, 4, 1, 0.33, 0.25 mmol) into 100 ml deionized water and stirring them for 1 h. Electrodeposition was carried out in a three electrode system as described above using the potential static technique at −1.0 V for 20 min at room temperature; the corresponding electrodes are denoted as $Ni(OH)_2 \cdot 0.75H_2O$–CeO_2 (2.5 : 1) NSs, $Ni(OH)_2 \cdot 0.75H_2O$–CeO_2 (10 : 1) NSs, $Ni(OH)_2 \cdot 0.75H_2O$–CeO_2 (30 : 1) NSs, and $Ni(OH)_2 \cdot 0.75H_2O$–CeO_2 (40 : 1) NSs, respectively. For the synthesis of $Ni(OH)_2 \cdot 0.75H_2O$ NSs, the method is similar to that of $Ni(OH)_2.0.75H_2O$–CeO_2 NSs without adding the $Ce(NO_3)_3 \cdot 6H_2O$ into the electrolyte. After deposition, the as-prepared products were washed with deionized water and absolute ethanol and then dried at 60 °C for 10 h. The mass loading of the products on CFP was approximately 6.8, 4.2, 7.5, 5.9, and 5.3 mg cm^{-2} for $Ni(OH)_2 \cdot 0.75H_2O$–CeO_2 (2.5 : 1) NSs, $Ni(OH)_2 \cdot 0.75H_2O$–CeO_2 (10 : 1) NSs, $Ni(OH)_2 \cdot 0.75H_2O$–CeO_2 (30 : 1) NSs, $Ni(OH)_2$-$\cdot 0.75H_2O$–CeO_2 (40 : 1) NSs and $Ni(OH)_2 \cdot 0.75H_2O$ NSs, respectively. These results were obtained by weighing the electrodes carefully before and after deposition.

Characterization

The morphology of the samples was characterized with field-emission scanning electron microscopy (FE-SEM, S-4800, Hitachi) and transmission electron microscopy (TEM, Tecnai G2 F30 S-TWIN, FEI). Powder X-ray diffraction (XRD) patterns were recorded on a Bruker D8 Advance diffractometer with Cu Kα radiation (λ = 1.5406 Å). The surface characteristics of the samples were investigated using ESCALAB250Xi X-ray photoelectron spectrometer (XPS).

Electrochemical measurement

Electrochemistry measurements were carried out on an electrochemistry workstation (CHI 760E, CH Instrument) in a three-port glass chamber. A mercury–mercury oxide electrode (MOE) was used as a reference electrode, and a graphite rod was used as a counter electrode. The counter electrode was separated from the chamber of working electrode by a porous glass frit. The electrolyte is an aqueous KOH solution (1 M). The RHE was determined by the open circuit potential of a clean Pt electrode in the solution of interest bubbled with H_2 (99.999%). A scan rate of 5 mV S^{-1} was adopted for the measurement of polarization curves. The measured potentials were corrected with ohmic drop (*iR*), where *i* is the current corresponding to the experimental potential and *R* is the uncompensated cell resistance estimated by current interrupt method. The apparent Tafel slope was derived from the *iR*-corrected polarization curve by fitting experimental data to the equation $\eta = a + b \log j$, where η is the *iR*-corrected potential, *a* is the Tafel constant, *b* is the Tafel slope, and *j* is the current density. Electrochemical impedance spectroscopy (EIS) were carried out at 1.55 V *vs.* RHE in the frequency range of 10^{-2} to 10^6 Hz with 10 mV sinusoidal perturbations and 12 steps per decade. Faradaic efficiency was measured by a method reported in our previous publications.[39–41]

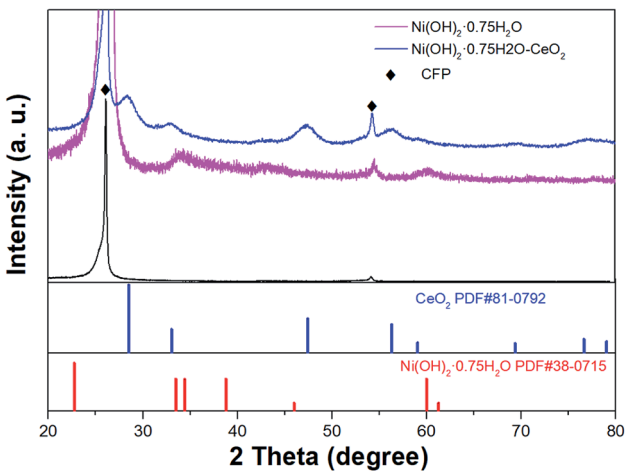

Fig. 1 XRD patterns of $Ni(OH)_2 \cdot 0.75H_2O$, $Ni(OH)_2 \cdot 0.75H_2O$–CeO_2 and bare CFP.

Results and discussion

The XRD pattern was recorded to determine the component of products. Fig. 1 gives the XRD pattern of the two samples resulted from electro-deposition, including $Ni(OH)_2 \cdot 0.75H_2O$ and $Ni(OH)_2 \cdot 0.75H_2O$–CeO_2. In spite of the poor crystallinity of the deposited samples, both of the two XRD patterns have a number of peaks that can be indexed to $Ni(OH)_2 \cdot 0.75H_2O$. The presence of $Ni(OH)_2 \cdot 0.75H_2O$ NSs were further examined using the HRTEM images. The detailed elemental composition and oxidation state of the hybrid arrays were further characterized using XPS analysis. The diffraction pattern for the as-prepared porous $Ni(OH)_2 \cdot 0.75H_2O$–CeO_2 NSs arrays on CFP, represented by the purple line, has seven obvious peaks at 28.5°, 33.0°, 47.5°, 56.3°, 59.0°, 69.4°, 76.7° and 79.0°, corresponding to (1 1 1), (2 0 0), (2 2 0), (3 1 1), (2 2 2), (4 0 0), (3 3 1), and (4 2 0) of cubic CeO_2 (JCPDS PDF81-0792). It is therefore suggested that CeO_2 was successfully doped into the $Ni(OH)_2 \cdot 0.75H_2O$ NSs. Owing to $Ni(OH)_2 \cdot 0.75H_2O$ NSs and $Ni(OH)_2 \cdot 0.75H_2O$–CeO_2 NSs growth on the CFP, peaks corresponding to the CFP were labeled by rhomboids.

The morphologies of NSs of $Ni(OH)_2 \cdot 0.75H_2O$ and $Ni(OH)_2 \cdot 0.75H_2O$–CeO_2 supported by CFP were examined with the SEM. Fig. 2a and b show that $Ni(OH)_2 \cdot 0.75H_2O$–CeO_2 nanosheets were homogenously deposited on the surface of CFP with a three-dimensional (3D) open structure. Cracks can be found on the surface of CFP (shown in the Fig. S1†), with a width of 1.6 μm, which may be due to drying in the oven. The thickness of the sample on the surface of CFP was estimated to be 3 μm, according to the crack exposing the cross-section of the sample (shown in the Fig. S1†). Energy-dispersive X-ray spectroscopy (EDX) confirms the presences of Ni, Ce and O in the $Ni(OH)_2 \cdot 0.75H_2O$–CeO_2 NSs (Fig. S2 in the ESI†). With increasing Ce concentration, the atomic ratio of Ni to Ce changes from 4.1 : 1 to 2.6 : 1 to 2.27 : 1 to 1.1 : 1 (shown in the Table S1†), of which the values were determined by ICP-MS. The microstructures of $Ni(OH)_2 \cdot 0.75H_2O$–CeO_2 NSs were further assessed by TEM. Fig. 2c shows a high resolution TEM (HRTEM) image of $Ni(OH)_2 \cdot 0.75H_2O$–CeO_2 NSs, which shows well-resolved lattice fringes with an inter-plane distance of 0.27 nm, which corresponds to the (200) plane of CeO_2, indicating the successfully introduction of CeO_2 in the composite. And the part of the lattice that is not obvious corresponds to $Ni(OH)_2 \cdot 0.75H_2O$, which is the same as HRTEM images of $Ni(OH)_2 \cdot 0.75H_2O$ NSs (Fig. S4a in the ESI†). The dark-field STEM image and the corresponding EDS mapping of the $Ni(OH)_2 \cdot 0.75H_2O$–CeO_2 NSs are shown in Fig. 2d–f. The element-mapping images of Ce, Ni, and O further confirm the Ni and Ce are homogeneously mixed with each other. For comparison, the pure $Ni(OH)_2 \cdot 0.75H_2O$ NSs grown on CFP was also synthesized by the same electro-deposition method without Ce source. The morphology of $Ni(OH)_2 \cdot 0.75H_2O$ NSs is analogous to that of $Ni(OH)_2 \cdot 0.75H_2O$–CeO_2 NSs, as shown by SEM images (Fig. S3 and S4 in the ESI†).

To demonstrate the activity of Ce for OER, the polarization curves were measured. The catalytic activity of $Ni(OH)_2 \cdot 0.75H_2O$–CeO_2 NSs and $Ni(OH)_2 \cdot 0.75H_2O$ NSs grown on CFP electrodes were studied initially by linear sweep voltammetry (LSV) in a standard three-electrode cell. A graphite rod was adopted as a counter electrode. All measured potentials were corrected with *iR* drop. Fig. 3a shows that the polarization curves of $Ni(OH)_2 \cdot 0.75H_2O$ and $Ni(OH)_2 \cdot 0.75H_2O$–CeO_2 with different atomic ratio of Ni to Ce. The overpotential required for a current density of 100 mA cm^{-2} (η_{100}) is 460 mV for $Ni(OH)_2 \cdot 0.75H_2O$ NSs. Once Ce source was doped into the samples, the η_{100} of these $Ni(OH)_2 \cdot 0.75H_2O$ NSs changes with

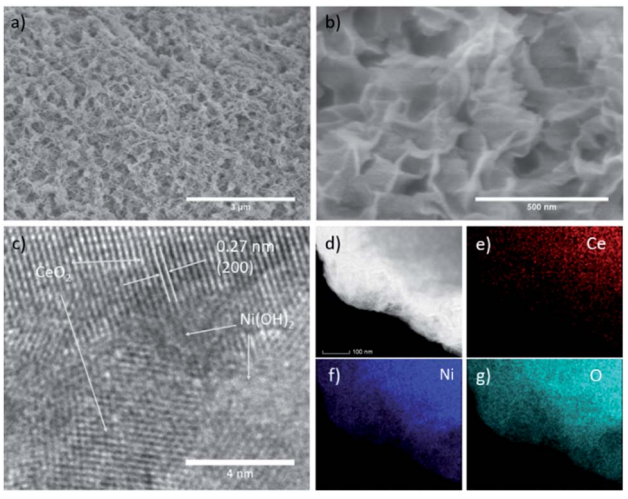

Fig. 2 (a and b) SEM images of $Ni(OH)_2 \cdot 0.75H_2O$–CeO_2. (c) HRTEM images of $Ni(OH)_2 \cdot 0.75H_2O$–CeO_2. (d) Dark-field STEM image of $Ni(OH)_2 \cdot 0.75H_2O$–CeO_2 and corresponding elemental mapping images of (e) Ce, (f) Ni, (g) O.

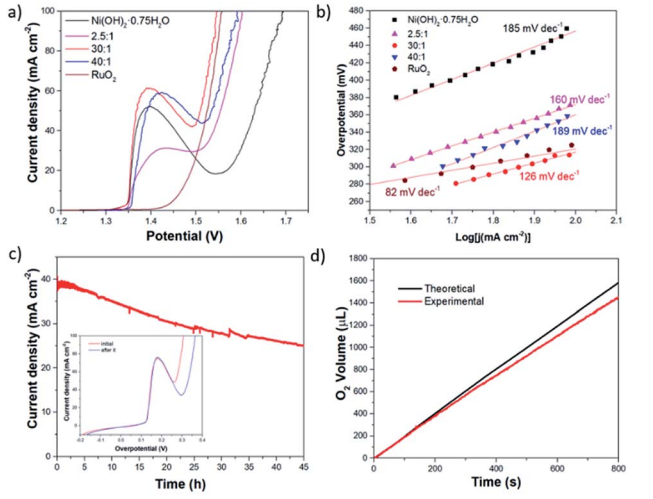

Fig. 3 The electrocatalytic performance of the catalysts. (a) Polarization curves and (b) Tafel of $Ni(OH)_2 \cdot 0.75H_2O$–CeO_2 (2.5 : 1), $Ni(OH)_2 \cdot 0.75H_2O$–CeO_2 (30 : 1), $Ni(OH)_2 \cdot 0.75H_2O$–CeO_2 (40 : 1), $Ni(OH)_2 \cdot 0.75H_2O$ and RuO_2 (c) current–time curve of $Ni(OH)_2 \cdot 0.75H_2O$–CeO_2 (30 : 1) recorded in a potentiostatic electrolysis experiment. Inset of (c) shows the LSV curves measured before and after potentiostatic electrolysis experiment. (d) Comparison of theoretical and detected volume of oxygen generated from a potentiostatic electrolysis. All potentials are corrected with *iR* drop.

a huge decrease. With the increased atomic ratio of Ni to Ce, the OER activity appears as volcano-like trend, in which the $Ni(OH)_2 \cdot 0.75H_2O$–CeO_2 (30 : 1) NSs endows the best OER performance among the tested catalysts. The η_{100} is as small as 320 mV, making it among the best OER catalysts (shown in the Table S2†). To gain more insight on the OER activity, Tafel plots derived from polarization curves were constructed (Fig. 3b). The resulting Tafel slope of $Ni(OH)_2 \cdot 0.75H_2O$–CeO_2 (30 : 1) NSs was 126 mV dec^{-1}, which is smaller than that of $Ni(OH)_2 \cdot 0.75H_2O$ NSs (185 mV dec^{-1}), $Ni(OH)_2 \cdot 0.75H_2O$–CeO_2 (40 : 1) NSs (189 mV dec^{-1}), and $Ni(OH)_2 \cdot 0.75H_2O$–CeO_2 (2.5 : 1) NSs (160 mV dec^{-1}), indicating that the $Ni(OH)_2 \cdot 0.75H_2O$–CeO_2 (30 : 1) NSs exhibited better OER activity.

Long-term stability in oxygen generation is the prerequisite of a practically useful OER catalyst. The long-term stability of the $Ni(OH)_2 \cdot 0.75H_2O$–CeO_2 NSs was demonstrated by the chronoamperometry. The $Ni(OH)_2 \cdot 0.75H_2O$–CeO_2 (30 : 1) NSs can maintain 64% of its capability in catalyzing the OER in long-term water electrolysis after 45 hours, shown in Fig. 3c. And, the η_{100} is increased from 310 mV to 365 mV after the long-time electrolysis test (the inset plot in Fig. 3c). The decay of η_{100} is about 18%. The SEM images of $Ni(OH)_2 \cdot 0.75H_2O$–CeO_2 (30 : 1) NSs subjected to long-term potentiostatic electrolysis is shown in Fig. S5 in the ESI,† which shows that most $Ni(OH)_2 \cdot 0.75H_2O$–CeO_2 (30 : 1) NSs maintain their 3D open structure with some nanosheets peeling off on the surface of the catalyst. EDX shows that the atomic ratio of Ni to Ce changes from 6.29 : 1 to 10.24 : 1 with some loss of Ce (Fig. S6 in the ESI†), which may be one of the reasons for degradation of catalyst performance.

The faradaic efficiency of $Ni(OH)_2 \cdot 0.75H_2O$–CeO_2 (30 : 1) NSs during O_2 evolution was evaluated by the comparison of the volume of generated gas and the theoretical volume in the potentiostatic electrolysis measurement, shown in Fig. 3d. The theoretical volumes were computed by assuming that all electrons passing through the circuit participate in the oxidation reaction of OH^- ($4OH^- - 4e^- \rightarrow O_2\uparrow + 2H_2O$), and the experiment volume was detected by the water displacement method. During electrolysis for 4000 s, the experiment and theoretical volumes are in good accordance, suggesting 92% faradaic efficiency.

To understand the excellent OER activity, EIS was tested at the potential of 1.55 V *vs.* RHE. The results are shown in the Nyquist curves in the Fig. 4a, where the data were fit using an equivalent circuit shown in Fig. S7 and Table S3 in the ESI.† The semicircle in the low frequency range is related to the faradaic process (OER) on electrocatalyst surface. Corresponding resistance element is charge transfer resistance (R_{ct}). R_{ct} is usually used as an indicator of OER kinetics, a smaller R_{ct} corresponds to a faster OER process. As shown in the Fig. 4a, the R_{ct} is decreased with the introduction of Ce to $Ni(OH)_2 \cdot 0.75H_2O$ NSs, and the R_{ct} of $Ni(OH)_2 \cdot 0.75H_2O$–CeO_2 (30 : 1) NSs (0.856 Ω) is smaller than those of $Ni(OH)_2 \cdot 0.75H_2O$ NSs (1.317 Ω), $Ni(OH)_2 \cdot 0.75H_2O$–CeO_2 (10 : 1) NSs (0.928 Ω), $Ni(OH)_2 \cdot 0.75H_2O$–CeO_2 (40 : 1) NSs (0.948 Ω) and $Ni(OH)_2 \cdot 0.75H_2O$–CeO_2 (2.5 : 1) NSs (1.177 Ω) under the same condition, suggesting that $Ni(OH)_2 \cdot 0.75H_2O$–CeO_2 (30 : 1) NSs possesses the fast electron transport ability for OER.

Electrochemically active surface area (ECSA) should play an important role in the high electrocatalytic performance, and it was derived from the specific capacitance measured by cyclic voltammetry (CV) scans (Fig. S8 in the ESI†). The potential range of the CV scans was selected at 1.1–1.2 V *vs.* RHE which did not include obvious electrochemical features corresponding to faradaic current. As a result, the dependence of the current on the scan rate in this region for both electrodes was linear. The ECSA of the $Ni(OH)_2 \cdot 0.75H_2O$ NSs, $Ni(OH)_2 \cdot 0.75H_2O$–CeO_2 (30 : 1) NSs, Ni $(OH)_2 \cdot 0.75H_2O$–CeO_2 (40 : 1) NSs, $Ni(OH)_2 \cdot 0.75H_2O$–CeO_2 (10 : 1) NSs, and $Ni(OH)_2 \cdot 0.75H_2O$–CeO_2 (2.5 : 1) NSs were measured to be 3.4 cm^2, 7.74 cm^2, 6.33 cm^2, 7.67 cm^2, and 5.83 cm^2 (shown in Fig. 4b). The ECSA of $Ni(OH)_2 \cdot 0.75H_2O$–CeO_2 (30 : 1) NSs is 2.3 times that of $Ni(OH)_2 \cdot 0.75H_2O$ NSs, demonstrating that the introduction of Ce can remarkably enlarge the ECSA of $Ni(OH)_2 \cdot 0.75H_2O$ NSs.

To understand the better intrinsic OER performance of $Ni(OH)_2 \cdot 0.75H_2O$–CeO_2 NSs, the activation energy of the OER was determined by Arrhenius plot: $\log(j) = -0.434E_a/(RT) + \text{const}$, where R is the Boltzmann constant (8.315 J g^{-1} mol^{-1} K^{-1}), E_a is the activation energy expressed in J g^{-1} mol^{-1}. Temperature related polarization curves of $Ni(OH)_2 \cdot 0.75H_2O$–CeO_2 (30 : 1) NSs and $Ni(OH)_2 \cdot 0.75H_2O$ NSs are shown in Fig. S9 in the ESI,† and corresponding Arrhenius plot at $\eta = 150$ mV can be found in the Fig. 5a. The E_a is 6.06 kJ mol^{-1} for $Ni(OH)_2 \cdot 0.75H_2O$–CeO_2 (30 : 1) NSs and 9.77 kJ mol^{-1} for $Ni(OH)_2 \cdot 0.75H_2O$ NSs. That is the $Ni(OH)_2 \cdot 0.75H_2O$–CeO_2

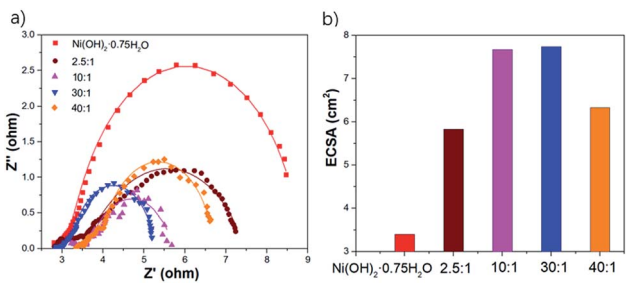

Fig. 4 (a) The Nyquist curves, (b) the ECSA of different samples.

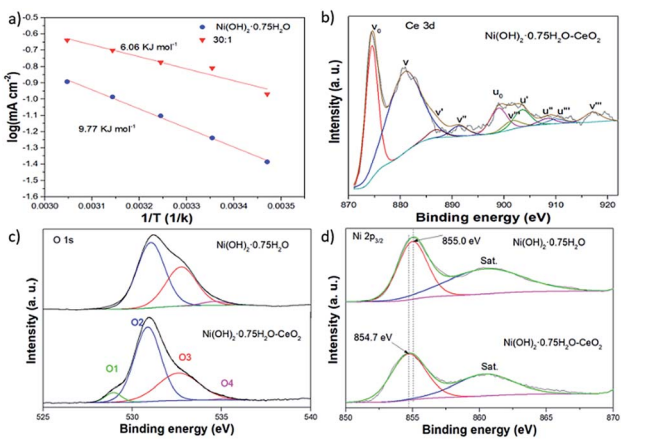

Fig. 5 (a) Arrhenius plots of $Ni(OH)_2 \cdot 0.75H_2O$ and $Ni(OH)_2 \cdot 0.75H_2O$–CeO_2 (30 : 1), (b–d) XPS spectra of Ce 3d, O 1s, and Ni 2p.

(30 : 1) NSs has a smaller apparent barrier height in the OER than $Ni(OH)_2 \cdot 0.75H_2O$ NSs.

In order to analyze the chemical composition of the prepared $Ni(OH)_2 \cdot 0.75H_2O$ NSs and $Ni(OH)_2 \cdot 0.75H_2O$–CeO_2 NSs electrocatalysts and to identify the chemical states of Ni, Ce, O elements in the samples, XPS measurements were carried out. As shown in Fig. 5b, XPS demonstrates that the element Ce mainly exists as CeO_2, which is composed of $3d_{5/2}$ (v_n) and $3d_{3/2}$ (u_n) spin–orbit components.[30] For Ce 3d of CeO_2, the spectra can be deconvoluted into 10 peaks, which consist of two pairs of doublets (v_0/u_0 and v'/u') assigned to Ce^{3+} and three pairs of doublets (v/u, v''/u'', and v'''/u''') assigned to Ce^{4+}, indicating the coexistence of Ce^{3+} and Ce^{4+} in the $Ni(OH)_2 \cdot 0.75H_2O$–CeO_2 NSs.[42,43] For the O 2p spectra (shown in Fig. 5c), peaks located at 530.87(O2), 832.60(O3) and 535.07(O4) eV are ascribed to the lattice oxygen, oxygen defects, and adsorbed oxygen species (water molecules), accordingly.[44–47] Meanwhile, a peak near 528.94 eV is usually attributed to lattice Ce–O,[30] reconfirming the existence of CeO_2. As shown in the Ni $2p_{3/2}$ spectra (Fig. 5d), the XPS results demonstrate that the element Ni of $Ni(OH)_2 \cdot 0.75H_2O$ NSs and $Ni(OH)_2 \cdot 0.75H_2O$–CeO_2 NSs mainly exist as $Ni(OH)_2$, containing Ni(II) species. However, there is a negative shift of 0.3 eV for Ni $2p_{3/2}$ in the $Ni(OH)_2 \cdot 0.75H_2O$–CeO_2 NSs, compared to those in the $Ni(OH)_2 \cdot 0.75H_2O$ NSs. Owing to the remarkable redox property of CeO_2,[48,49] This result suggests the electron transfer between $Ni(OH)_2$ and CeO_2, contributing to a strong electron interaction formed between $Ni(OH)_2$ and CeO_2, and accordingly enhancing the electrocatalytic performance.

Conclusions

In summary, cerium doped nickel hydroxide NSs were directly electrodeposited on CFP, and it exhibited superior OER activity compared to nickel hydroxide nanosheets. With the introduction of Ce, the optimized $Ni(OH)_2 \cdot 0.75H_2O$–CeO_2 NSs showed a tremendous increase in OER performance with the smallest η_{100} of 320 mV and Tafel slope of 126 mV dec^{-1} in alkaline electrolyte, as compared with that of $Ni(OH)_2 \cdot 0.75H_2O$ NSs deposited in the same electrodeposition method. Meanwhile, the catalyst is stable for 45 h at high current density and 92% faradaic efficiency. The introduction of Ce brings strong electronic interactions between $Ni(OH)_2$ and CeO_2 and more electrochemically active sites, which should play an essential role in enhancing the OER activity.

Conflicts of interest

There are no conflicts to declare.

Acknowledgements

This research was financially supported by the National Natural Science Foundation of China (51772214, 51432006), the Ministry of Science and Technology of China (2011DFG52970), the Ministry of Education of China (IRT14R23), 111 Project (B13025), Jiangsu Province (2011-XCL-019 and 2013-479).

References

1 S. Chu and A. Majumdar, *Nature*, 2012, **488**, 294.
2 R. Schloegl, *Nat. Mater.*, 2008, **7**, 772.
3 M. S. Dresselhaus and I. L. Thomas, *Nature*, 2001, **414**, 332.
4 A. J. Bard and M. A. Fox, *Acc. Chem. Res.*, 1995, **28**, 141.
5 M. G. Walter, E. L. Warren, J. R. McKone, S. W. Boettcher, Q. Mi, E. A. Santori and N. S. Lewis, *Chem. Rev.*, 2010, **110**, 6446.
6 C. C. McCrory, S. Jung, I. M. Ferrer, S. M. Chatman, J. C. Peters and T. F. Jaramillo, *J. Am. Chem. Soc.*, 2015, **137**, 4347–4357.
7 I. Markoulaki, I. Papadas, I. Kornarakis and G. Armatas, *Nanomaterials*, 2015, **5**, 1971–1984.
8 X. Long, J. Li, S. Xiao, K. Yan, Z. Wang, H. Chen and S. Yang, *Angew. Chem., Int. Ed.*, 2014, **53**(29), 7584–7588.
9 T. Sharifi, E. Gracia-Espino, X. Jia, R. Sandstrom and T. Wågberg, *ACS Appl. Mater. Interfaces*, 2015, **7**(51), 28148–28155.
10 L. J. Foruzin, Z. Rezvani, Y. H. Shishavan and B. Habibi, *Int. J. Hydrogen Energy*, 2018, **43**(1), 150–160.
11 J. Li, G. Liu, B. Liu, Z. Min, D. Qian, J. Jiang and J. Li, *Int. J. Hydrogen Energy*, 2018, **43**(3), 1365–1374.
12 J. A. Koza, Z. He, A. S. Miller and J. A. Switzer, *Chem. Mater.*, 2012, **24**(18), 3567–3573.
13 R. Chen, H. Y. Wang, J. Miao, H. Yang and B. Liu, *Nano Energy*, 2015, **11**, 333–340.
14 X. Zheng, B. Zhang, P. De Luna, Y. Liang, R. Comin, O. Voznyy and T. Regier, *Nat. Chem.*, 2018, **10**(2), 149.
15 R. D. Smith, M. S. Prévot, R. D. Fagan, S. Trudel and C. P. Berlinguette, *J. Am. Chem. Soc.*, 2013, **135**(31), 11580–11586.
16 B. Zhang, X. Zheng, O. Voznyy, R. Comin, M. Bajdich, M. García-Melchor and F. P. G. de Arquer, *Science*, 2016, **352**(6283), 333–337.
17 R. Subbaraman, D. Tripkovic, K. C. Chang, D. Strmcnik, A. P. Paulikas, P. Hirunsit and N. M. Markovic, *Nat. Mater.*, 2012, **11**(6), 550.
18 J. W. D. Ng, M. García-Melchor, M. Bajdich, P. Chakthranont, C. Kirk, A. Vojvodic and T. F. Jaramillo, *Nat. Energy*, 2016, **1**(5), 16053.
19 F. Dionigi and P. Strasser, *Adv. Energy Mater.*, 2016, **6**(23), 1600621.
20 L. Han, S. J. Dong and E. K. Wang, *Adv. Mater.*, 2016, **28**, 9266.
21 C.-C. Lin and C. C. L. McCrory, *ACS Catal.*, 2017, **7**, 443.
22 T. Tang, W.-J. Jiang, S. Niu, N. Liu, H. Luo, Y.-Y. Chen, S.-F. Jin, F. Gao, L.-J. Wan and J.-S. Hu, *J. Am. Chem. Soc.*, 2017, **139**, 8320.
23 G. Wu, W. X. Chen, X. S. Zheng, D. P. He, Y. Q. Luo, X. Q. Wang, J. Yang, Y. E. Wu, W. S. Yan, Z. B. Zhuang, X. Hong and Y. D. Li, *Nano Energy*, 2017, **38**, 167.
24 J. X. Feng, H. Xu, Y. T. Dong, S. H. Ye, Y. X. Tong and G. R. Li, *Angew. Chem., Int. Ed.*, 2016, **55**(11), 3694–3698.
25 X. F. Lu, L. F. Gu, J. W. Wang, J. X. Wu, P. Q. Liao and G. R. Li, *Adv. Mater.*, 2017, **29**(3), 1604437.

26 S. H. Ye, Z. X. Shi, J. X. Feng, Y. X. Tong and G. R. Li, *Angew. Chem., Int. Ed.*, 2018, **57**(10), 2672–2676.
27 J. A. Haber, Y. Cai, S. Jung, C. X. Xiang, S. Mitrovic, J. Jin, A. T. Bell and J. M. Gregoire, *Energy Environ. Sci.*, 2014, **7**, 682.
28 Y.-R. Zheng, M.-R. Gao, Q. Gao, H.-H. Li, J. Xu, Z.-Y. Wu and S.-H. Yu, *Small*, 2015, **11**, 182.
29 J. W. D. Ng, M. García-Melchor, M. Bajdich, P. Chakthranont, C. Kirk, A. Vojvodic and T. F. Jaramillo, *Nat. Energy*, 2016, **1**, 16053.
30 J.-X. Feng, S.-H. Ye, H. Xu, Y.-X. Tong and G.-R. Li, *Adv. Mater.*, 2016, **28**, 4698.
31 Z. Q. Liu, N. Li, H. Y. Zhao, Y. Zhang, Y. H. Huang, Z. Y. Yin and Y. P. Du, *Chem. Sci.*, 2017, **8**, 3211.
32 W. Gao, M. Yan, H.-Y. Cheung, Z. M. Xia, X. M. Zhou, Y. B. Qin, C.-Y. Wong, J. C. Ho, C.-R. Chang and Y. Q. Qu, *Nano Energy*, 2017, **38**, 290.
33 X. Wang, Y. Yang, L. Diao, Y. Tang, F. He, E. Liu and S. Ji, *ACS Appl. Mater. Interfaces*, 2018, **10**(41), 35145–35153.
34 M. Favaro, W. S. Drisdell, M. A. Marcus, J. M. Gregoire, E. J. Crumlin, J. A. Haber and J. Yano, *ACS Catal.*, 2017, **7**(2), 1248–1258.
35 W. Gao, Z. Xia, F. Cao, J. C. Ho, Z. Jiang and Y. Qu, *Adv. Funct. Mater.*, 2018, **28**(11), 1706056.
36 K. Obata and K. Takanabe, *Angew. Chem., Int. Ed.*, 2018, **57**(6), 1616–1620.
37 S. Xu, C. Lv, T. He, Z. Huang and C. Zhang, *J. Mater. Chem. A*, 2019, **7**, 7526–7532.
38 H. Zhang, H. Ning, J. Busbee, Z. Shen, C. Kiggins, Y. Hua and J. M. Zuo, *Sci. Adv.*, 2017, **3**(5), e1602427.
39 C. Lv, Z. Huang, Q. Yang, G. Wei, Z. Chen, M. G. Humphrey and C. Zhang, *J. Mater. Chem. A*, 2017, **5**, 22805–22812.
40 C. Lv, Q. Yang, Q. Huang, Z. Huang, H. Xia and C. Zhang, *J. Mater. Chem. A*, 2016, **4**, 13336–13343.
41 L. Jin, H. Xia, Z. Huang, C. Lv, J. Wang, M. G. Humphrey and C. Zhang, *J. Mater. Chem. A*, 2016, **4**, 10925–10932.
42 C. Hardacre, G. M. Roe and R. M. Lambert, *Surf. Sci.*, 1995, **326**(1–2), 1–10.
43 B. Lin, Y. Liu, L. Heng, J. Ni, J. Lin and L. Jiang, *Catal. Commun.*, 2017, **101**, 15–19.
44 W. X. Guo, W. W. Sun and Y. Wang, *ACS Nano*, 2015, **9**, 11462.
45 T. V. Thi, A. K. Rai, J. Gim and J. Kim, *J. Power Sources*, 2015, **292**, 23.
46 B. P. Payne, M. C. Biesigner and N. S. McIntyre, *J. Electron Spectrosc. Relat. Phenom.*, 2012, **185**, 159.
47 J. Bao, X. D. Zhang, B. Fan, J. J. Zhang, M. Zhou, W. L. Yang, X. Hu, H. Wang, B. C. Pan and Y. Xie, *Angew. Chem.*, 2015, **127**, 7507.
48 C. T. Campbell and C. H. F. Peden, *Science*, 2005, **309**, 713.
49 J. Paier, C. Penschke and J. Sauer, *Chem. Rev.*, 2013, **113**, 3949.